Dynamic Mode Decomposition Based Reduced-Order Temperature Field Prediction Method for IGBT Module

Jiahao Geng, Fujin Deng, *Senior Member, IEEE*, Kai Hou, Qiang Yu, Yaqian Zhang, *Member, IEEE*, Yeyuan Xie, Jun Mei, *Member, IEEE*, and Guangtai Zhang

***Abstract*—Detailed temperature field distribution of high-power insulated gate bipolar transistor (IGBT) modules is essential information for reliability analysis and thermal design of power electronic systems. This article proposes a dynamic mode decomposition (DMD) based reduced-order temperature field prediction method for IGBT module. The IGBT temperature field (ITF) snapshot data obtained from finite element method simulation are decomposed to obtain the dynamic modes. And then, the dominant modes among dynamic modes are chosen to establish a reduced-order model, which can quickly predict the ITF. The proposed DMD based RTFP method only requires a small number of sample snapshots to capture the dynamic modes of ITF and selects a small number of dominant modes to predict the ITF, and accordingly it improves the computational efficiency and reduces the disk space occupation. In addition, it does not require complex mathematical models and can obtain detailed ITF distribution. Finally, the accuracy of the proposed method is verified by simulation and experiment.**

***Index Terms*—Dynamic mode decomposition (DMD), finite element method (FEM), insulate-gate bipolar transistor (IGBT), temperature field prediction.**

I. Introduction

INSULATED gate bipolar transistor (IGBT), known for its simple drive control, high conduction current, and low conduction voltage, has become a core component of power converters [1], [2], [3], [4]. However, the failure of the IGBT can lead to power interruptions and unexpected shutdowns, resulting in serious economic consequences [5]. The IGBT temperature field (ITF) directly affects its performance, operational safety, and long-term reliability. Particularly, common failure mechanisms, such as bond wire lift-off and solder layer fatigue, are closely related to the ITF [6]. Therefore, accurate prediction of the ITF is crucial for improving reliability prediction and health management.

To predict the ITF, three typical methods are used: measurement methods, thermal network models, and numerical methods. Measurement methods directly obtain the ITF through experiments, mainly including thermal sensor methods and infrared methods. The thermal sensor method relies on the temperature change characteristics of thermosensitive elements for measurement but requires full contact with the surface of the semiconductor chip [7]. In contrast, infrared methods use infrared temperature measuring devices to measure the junction temperature of the IGBT module without needing to contact the semiconductor chip, thus providing the temperature distribution of the entire chip surface. However, the thermal sensor methods may introduce additional thermal impedance, while infrared methods require opening the IGBT package, potentially damaging the device or affecting its performance [8]. Moreover, these direct measurement methods are invasive, inefficient, and challenging for data collection [9].

Thermal network models are easy to implement in circuit simulation software, offering relatively fast simulation speeds [10]. These models include Foster and Cauer models [11], typically represented by RC networks with thermal resistances and capacitances. The Foster thermal network model is a fitting model primarily used to calculate the temperature difference between the measurement point and a reference point, from which the measurement point's temperature is inferred. The Cauer thermal network model is based on the actual physical structure of power devices and simulates the thermal resistance of each layer of the power device material using a set of thermal capacitances and resistances, allowing for the calculation of the temperature of each layer. These thermal network models, due to their low complexity, can be applied in real time. However, these models do not consider factors such as thermal cross-coupling effects between chips and require re-modeling when boundary conditions change [12], [13]. Three-dimensional (3-D) thermal network models calculate junction temperature by summing the outputs of multiple Foster or Cauer models, with each model used to simulate the thermal cross-coupling effects of multiple

Received 12 November 2024; revised 26 February 2025 and 30 April 2025; accepted 26 May 2025. Date of publication 9 June 2025; date of current version 5 August 2025. This work was supported in part by the National Natural Science Foundation of China under Project 52277173 and Project U23B20137. Recommended for publication by Associate Editor A. Lindemann. *(Corresponding author: Fujin Deng.)*

Jiahao Geng, Fujin Deng, Qiang Yu, Yaqian Zhang, and Jun Mei are with the School of Electrical Engineering, Southeast University, Nanjing 210096, China (e-mail: gengjiahao@seu.edu.cn; fdeng@seu.edu.cn; yuqiang@seu.edu.cn; yqzh@seu.edu.cn; mei_jun@seu.edu.cn).

Kai Hou is with the NARI Group Corporation, State Grid Electric Power Research Institute, Nanjing 210003, China (e-mail: houkai@sgepri.sgcc.com.cn).

Yeyuan Xie is with the NR Electric Company Ltd., Nanjing 210096, China (e-mail: xieyy@nrec.com).

Guangtai Zhang is with the Changzhou Borui Power Automation Equipment Company Ltd., Changzhou 213000, China (e-mail: zhanggt@nrec.com).

Color versions of one or more figures in this article are available at https://doi.org/10.1109/TPEL.2025.3578106.

Digital Object Identifier 10.1109/TPEL.2025.3578106

semiconductor chips within the device [10], [11], [12], [13], [14]. However, 3-D thermal network models require multiple Foster or Cauer models to manually fit finite element simulation step response data, and the order of the generated model increases with the number of inputs and outputs.

Numerical methods are widely used to solve thermodynamic problems with complex geometries and boundary conditions, including the finite element method (FEM), finite difference method, and finite volume method. These methods handle strong thermal coupling effects in IGBT modules, providing high-precision temperature predictions [15]. Additionally, numerical methods can offer detailed internal temperature information of the module, which is crucial for analyzing IGBT module failure mechanisms. For example, reference [16] uses FEM to study the temperature response of chips under different solder layer degradation conditions, while reference [17] uses FEM to study temperature fluctuations at bond wire contacts. Furthermore, numerical methods are applied in the packaging and thermal design of IGBT modules to reduce experimental trials and lower costs [18], [19]. However, numerical models represented by FEM require solving tens of thousands or even millions of node equations, usually taking hours or even tens of hours of computation time, which limits their applicability.

To address the computational burden faced by FEM, this article proposes a dynamic mode decomposition (DMD) based reduced-order temperature field prediction (RTFP) method for IGBT modules. The ITF snapshot data from FEM simulation is decomposed to extract the dominant dynamic modes of ITF. Finally, the dominant modes are used to predict the ITF with a deficient error level. The primary contributions of the proposed method include the following.

1) The proposed method has almost the same prediction accuracy as FEM.
2) The proposed method significantly shortens the computation time of FEM and reduces the disk space for data storage.
3) The proposed method does not require the construction of complex mathematical models and has clear physical implications.
4) The proposed method can obtain the prediction of the entire ITF distribution, not just the junction temperature.

In conclusion, the proposed method can greatly improve the simulation efficiency for researchers.

The rest of this article is organized as follows. Section II describes the structure of the IGBT module. Section III proposes the DMD based RTFP method for the IGBT module. Section IV discusses the proposed method. Section V presents the experiment results. Finally, Section VI concludes this article.

II. IGBT Module Internal Structure

This article uses a commercial IGBT module FF300R12ME4 as a sample, rated at 1200 V and 300 A. Fig. 1 shows its physical structure. The module is a half-bridge comprising the upper arm and the lower arm. The upper arm contains three IGBT chips Q1–Q3 and three diode chips D1–D3 connected in parallel. The lower arm contains three IGBT chips Q4–Q6

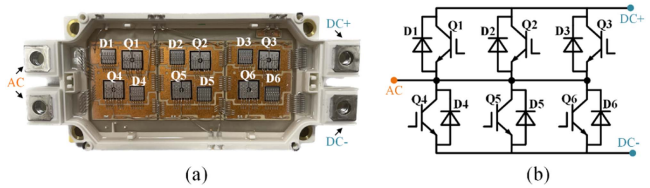

Fig. 1. Physical structure and circuit schematic of FF300R12ME4. (a) Physical structure. (b) Circuit schematic.

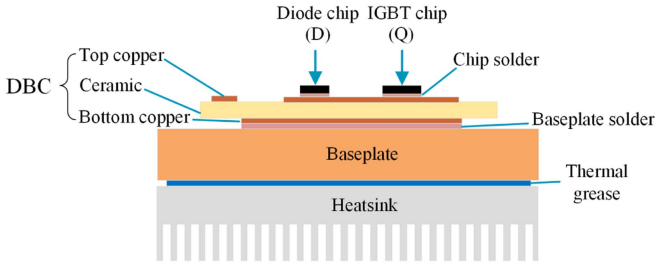

Fig. 2. Cross-sectional view of FF300R12ME4 with heat sink.

and three diode chips D4–D6 connected in parallel. Fig. 2 shows the cross-sectional of the IGBT module FF300R12ME4. The IGBT module packages are vertically layered structures composed of chip, chip solder, direct bond copper (DBC, which is composed of top copper, ceramic, bottom copper), baseplate solder, and baseplate components. The DBC provides excellent thermal conductivity. In practical applications, the module is mechanically fixed on the heat sink to enhance heat dissipation efficiency.

III. Proposed DMD Based Reduced-Order Temperature Field Prediction Method

The DMD is widely used for modes extraction of data in fluid dynamics, disease modeling, and finance due to its computational efficiency and excellent modes decomposition capability [20]. In this article, the DMD is adopted to capture the ITF dynamic modes, and a DMD-based RTFP method is proposed for IGBT module, as shown in Fig. 3, which includes Stage-1 (ITF data matrix capture), Stage-2 (ITF modes decomposition), and Stage-3 (ITF prediction). First, the temperature data matrix (TDM) is captured based on the ITF snapshots obtained from the FEM simulation. Second, the ITF dynamic modes are obtained based on the decomposition of the TDM. Third, the ITF prediction is obtained based on the dominant ITF dynamic modes.

A. Stage-1: ITF Data Matrix Capture

The ITF data are obtained based on the FEM simulation due to its realistic physical modeling and consideration of thermal coupling effects [4]. First, the dimensions of the components of the IGBT module (including the substrate, DBC, chips, etc.) and the heat sink are obtained from the manufacturer. Based on the obtained dimension information, a finite element model of the IGBT module FF300R12ME4 with heat sink is constructed in ANSYS, as shown in Fig. 4, ignoring geometrical structures that are not in the dissipation path. The detailed modeling process

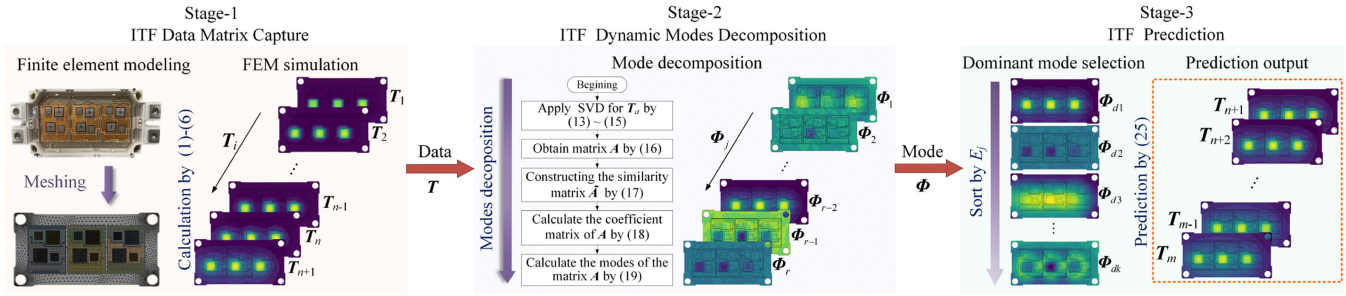

Fig. 3. Proposed RTFP method.

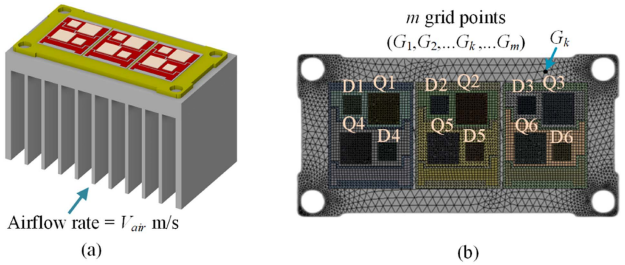

Fig. 4. Finite element model in ANSYS. (a) CAD model of FF300R12ME4 with heat sink. (b) 3-D meshing diagram of the FF300R12ME4.

TABLE I
MAJOR MATERIAL OF THE IGBT MODULE

Layers	Materials	ρ (kg/m^3)	K (w/(m·°C))	Cp (J/(kg/°C))
Chip	Si	2330	148	712
Solder	SnAgCu	7430	64	220
DBC copper	Cu	8993	400	385
Ceramic	AL2O3	3800	27	776
Baseplate	Cu	8993	400	385

can be referred to reference [4]. The heat sink uses forced air cooling with an airflow rate of V_{air} m/s. The FEM simulation is set up for fluid-structure coupling. Table I shows the material parameters of the IGBT model FF300R12ME4. In Table I, ρ is the material density, K is the material thermal conductivity, C_p is the material specific heat capacity. Here, the

IGBT model is meshed into m grid points based on the principle that thinner parts are meshing with finer elements [21], and the kth grid point is named as G_k.

In the FEM simulation, the chip (Q1–Q6, D1–D6) regions of the IGBT model are set as heat sources, and the power losses of the chips are loaded into the heat sources. To simplify the analysis, the power losses between parallel chips (for example, Q1–Q3) are considered to be evenly distributed, and the power loss P_x of chip x (x = Q1–Q6, D1–D6) can be expressed as follows:

$$P_x = \begin{cases} \frac{P_{\text{upper\_Q}}}{3}, x = \text{Q}_1, \text{Q}_2, \text{Q}_3 \\ \frac{P_{\text{lower\_Q}}}{3}, x = \text{Q}_4, \text{Q}_5, \text{Q}_6 \\ \frac{P_{\text{upper\_D}}}{3}, x = \text{D}_1, \text{D}_2, \text{D}_3 \\ \frac{P_{\text{lower\_D}}}{3}, x = \text{D}_4, \text{D}_5, \text{D}_6 \end{cases} \tag{1}$$

where $P_{\text{upper·Q}}$ is the total power loss of the three chips Q1–Q3, $P_{\text{lower·Q}}$ is the total power loss of the three chips Q4–Q6, $P_{\text{upper·D}}$ is the total power loss of the three chips D1–D3, $P_{\text{lower·D}}$ is the total power loss of the three chips D4–D6. In ANSYS, the power loss P_x is loaded into each chip in the form of internal heat generation rate H_{G} (W·mm^{-3}), which can be expressed as follows:

$$H_{\text{G}} = \frac{P_x}{V_x} \tag{2}$$

where V_x represents the volume of the chip x. Based on H_{G}, the temperature $T_{(k)}$ at G_k of the IGBT can be obtained by the following [22]:

$$\frac{\partial T_{(k)}}{\partial t} = \frac{\nabla \cdot (K \nabla T_{(k)}) + H_G}{\rho C_p} \tag{3}$$

where t is the simulation time, and ∇ is the gradient operator.

Normally, power cycling tests are conducted with a single switch consisting of chips connected in parallel [23]. Here, the lower switch in the IGBT module FF300R12ME4 consisting of Q4–Q6 is used as an example for ITF prediction. To simplify the actual transient power loss of the IGBT module in the inverter, an equivalent power loss curve is proposed to replace it [24], which is a sinusoidal half wave as

$$P_x = \begin{cases} P_{\text{peak}} \cdot \sin(2\pi f_{\text{p}} t) & P_x > 0 \\ 0 & P_x \le 0 \end{cases} \tag{4}$$

where P_{peak} is the amplitude, and f_{p} is the equivalent frequency.

Based on (1)–(4) and Table I, the ITF transient results, with $P_{\text{peak}} = 200$ W and $f_{\text{p}} = 50$ Hz as an example, can be obtained by FEM simulation. Based on the obtained ITF transient results with the FEM simulation, the IGBT temperature data of m grid points are sampled with the sampling interval of Δt, as shown in Fig. 5. At the ith sampling instant, the ith sample snapshot $\boldsymbol{T}_i$ can be obtained as follows:

$$\boldsymbol{T}_i = \begin{bmatrix} T_{i(1)} \\ T_{i(2)} \\ \cdots \\ T_{i(m)} \end{bmatrix} \tag{5}$$

where $T_{i(k)}$ is the temperature data of the grid point G_k ($1 \le k \le m$) at the ith sampling instant. The n+1 snapshots $\boldsymbol{T}_1 \sim \boldsymbol{T}_{(n+1)}$ are sampled with sampling range $S_t = (n+1)\Delta t$, to form the TDM

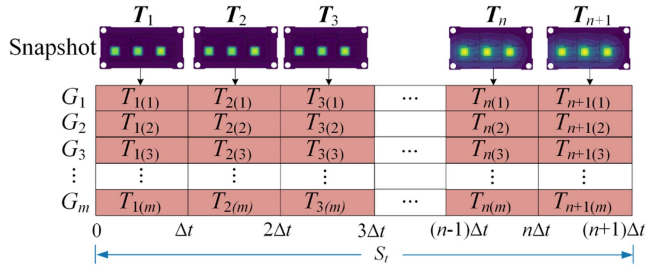

Fig. 5. ITF sampling snapshot.

$\boldsymbol{T}$ as follows:

$$\boldsymbol{T} = [\boldsymbol{T}_1 \boldsymbol{T}_2 \boldsymbol{T}_3 \ldots \boldsymbol{T}_i \ldots \boldsymbol{T}_{n+1}]. \tag{6}$$

B. Stage-2: ITF Dynamic Mode Decomposition

The DMD is a commonly used method to extract features of linear dynamic systems from sampling snapshots [20]. In this article, the DMD can be used to extract features of the ITF evolution process by sampling TDM $\boldsymbol{T}$. This is because the ITF evolution process can be regarded as a linear dynamic system when material parameter variations are disregarded. The output of the DMD is a set of dynamic modes that represent the features of the ITF evolution, which can be used subsequently for the ITF prediction.

With the DMD [25], TDM $\boldsymbol{T}$ is divided into two time-shifted TDMs $\boldsymbol{T}_\alpha$ and$\boldsymbol{T}_\beta$ as

$$\boldsymbol{T}_\alpha = [\boldsymbol{T}_1, \ldots, \boldsymbol{T}_i, \ldots, \boldsymbol{T}_n] \tag{7}$$

$$\boldsymbol{T}_\beta = [\boldsymbol{T}_2, \ldots, \boldsymbol{T}_{i+1} \ldots, \boldsymbol{T}_{n+1}] \tag{8}$$

and there exists a best-fit dynamic matrix $\boldsymbol{A}$ that can map $\boldsymbol{T}_\alpha$ to $\boldsymbol{T}_\beta$, which can be expressed as follows:

$$\boldsymbol{T}_\beta = \boldsymbol{A}\boldsymbol{T}_\alpha \tag{9}$$

with

$$\boldsymbol{T}_{i+1} = \boldsymbol{A}\boldsymbol{T}_i \tag{10}$$

and the dynamic matrix $\boldsymbol{A}$ in (10) can be decomposed into superposition of $r\,(1 \le r \le n)$ order of ITF dynamic mode $\boldsymbol{\Phi}_1$–$\boldsymbol{\Phi}_r$ as follows:

$$\boldsymbol{A} = \sum_{j=1}^{r} \lambda_j \boldsymbol{\Phi}_j \boldsymbol{\Phi}_j^{+} \tag{11}$$

where $\boldsymbol{\Phi}_j{}^{+}$ is the generalized inverse of $\boldsymbol{\Phi}_j$ $(j = 1, \ldots, r)$, λ_j is the coefficient of the mode $\boldsymbol{\Phi}_j$. The mode $\boldsymbol{\Phi}_j$ is associated with a specific frequency f_j as

$$f_j = \frac{\log(\mathrm{Im}(\lambda_j))/\Delta t}{2\pi}. \tag{12}$$

According to the DMD [25], when the number n+1 of sample snapshots is sufficiently large, the modes $\boldsymbol{\Phi}_1$–$\boldsymbol{\Phi}_r$ can capture the main trends in the ITF evolution and be used for short-term ITF prediction. Based on (7)–(11), the decomposition process of dynamic modes $\boldsymbol{\Phi}_1$–$\boldsymbol{\Phi}_r$ for the $\boldsymbol{A}$ is shown in Fig. 6, which includes the following Steps 1–5.

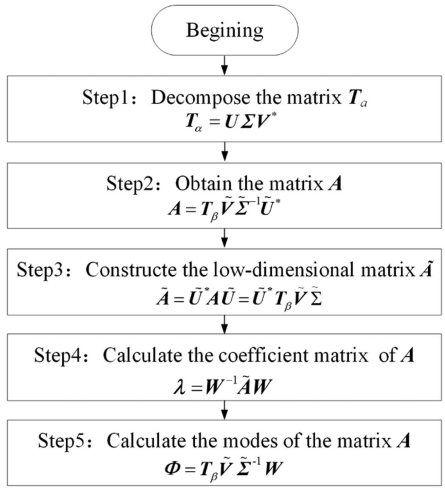

Fig. 6. Dynamic modes decomposition steps.

Step 1: To avoid dealing with the large-size matrix, singular value decomposition (SVD) is applied for TDM $\boldsymbol{T}_\alpha$ as follows:

$$\boldsymbol{T}_\alpha = \boldsymbol{U}\,\boldsymbol{\Sigma}\,\boldsymbol{V}^*. \tag{13}$$

Here, $\boldsymbol{U} \in \mathbb{C}^{m\times n}$ and $\boldsymbol{V} \in \mathbb{C}^{n\times n}$ are singular vector matrices that store the temporal and spatial modes of the ITF, respectively, and $*$ is the conjugate transpose. $\boldsymbol{\Sigma} \in \mathbb{C}^{n\times n}$ is the singular value diagonal matrix, as

$$\boldsymbol{\Sigma} = \mathrm{diag}[\sigma_1 \sigma_2 \ldots \sigma_i \ldots \sigma_n](\sigma_1 > \sigma_2 > \ldots > \sigma_n) \tag{14}$$

where σ_i is the singular value and represents the strength of the corresponding ITF temporal-spatial modes. To improve computational speed and capture the main ITF temporal–spatial dynamic modes, the r $(1 \le r \le n)$ largest singular values and the corresponding singular vectors are truncated. Then, TDM $\boldsymbol{T}_\alpha$ can be decomposed in low-dimension by truncated SVD, which can be expressed as follows:

$$\boldsymbol{T}_\alpha \approx \tilde{\boldsymbol{U}}\,\tilde{\boldsymbol{\Sigma}}\,\tilde{\boldsymbol{V}}^* \tag{15}$$

where $\tilde{\boldsymbol{U}} \in \mathbb{C}^{m\times r}$, $\tilde{\boldsymbol{V}} \in \mathbb{C}^{n\times r}$, and $\tilde{\sum} \in \mathbb{C}^{r\times r}$ are truncated matrix by $\boldsymbol{U}$, $\boldsymbol{V}$, and $\sum$.

Step 2: According to (9) and (15), the dynamic matrix$\boldsymbol{A}$ can be obtained as follows:

$$\boldsymbol{A} = \boldsymbol{T}_\beta \tilde{\boldsymbol{V}}\,\tilde{\boldsymbol{\Sigma}}^{-1}\,\tilde{\boldsymbol{U}}^*. \tag{16}$$

Step 3: The dynamic matrix $\boldsymbol{A}$ in (16) is projected onto $\tilde{\boldsymbol{U}}$ to obtain a similar low-dimension matrix $\tilde{\boldsymbol{A}}$ as

$$\tilde{\boldsymbol{A}} = \tilde{\boldsymbol{U}}^*\,\boldsymbol{A}\,\tilde{\boldsymbol{U}} = \tilde{\boldsymbol{U}}^*\,\boldsymbol{T}_\beta\,\tilde{\boldsymbol{V}}\,\tilde{\boldsymbol{\Sigma}}. \tag{17}$$

Step 4: According to the similarity property of matrices, the dynamic matrix $\boldsymbol{A}$ and $\tilde{\boldsymbol{A}}$ have the same coefficient matrix λ. Based on (17), the coefficient matrix λ of dynamic matrix $\boldsymbol{A}$

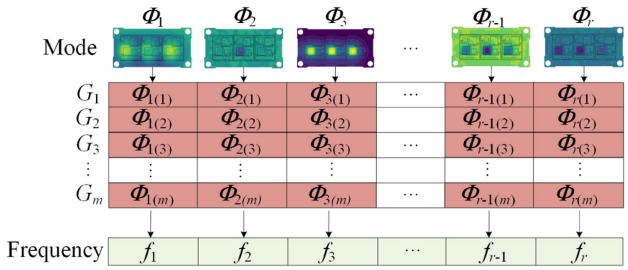

Fig. 7. Modes of the dynamic matrix $\boldsymbol{A}$.

can be obtained by spectral decomposition of $\widetilde{\boldsymbol{A}}$ as follows:

$$\begin{aligned}\boldsymbol{\lambda} &= \boldsymbol{W}^{-1}\,\widetilde{\boldsymbol{A}}\,\boldsymbol{W} \\ &= \mathrm{diag}[\lambda_1\lambda_2\ldots\lambda_j\ldots\lambda_r]\end{aligned} \tag{18}$$

where $\boldsymbol{W}$ is the eigenvector matrix of $\widetilde{\boldsymbol{A}}$.

Step 5: Based on (16) and (18), the modes matrix $\boldsymbol{\Phi} \in \mathbb{C}^{m\times r}$ of the dynamic matrix$\boldsymbol{A}$ can be obtained as follows:

$$\begin{aligned}\boldsymbol{\Phi} &= \boldsymbol{T}_\beta\,\widetilde{\boldsymbol{V}}\,\widetilde{\boldsymbol{\Sigma}}^{-1}\,\boldsymbol{W} \\ &= [\boldsymbol{\Phi}_1\boldsymbol{\Phi}_2\ldots\boldsymbol{\Phi}_j\ldots\boldsymbol{\Phi}_r]\end{aligned} \tag{19}$$

with

$$\boldsymbol{\Phi}_j = \begin{bmatrix}\boldsymbol{\Phi}_{j(1)}\\ \boldsymbol{\Phi}_{j(2)}\\ \ldots\\ \boldsymbol{\Phi}_{j(m)}\end{bmatrix}. \tag{20}$$

Based on Steps 1–5, Fig. 7 shows the dynamic matrix $\boldsymbol{A}$ is decomposed into r number of modes $\boldsymbol{\Phi}_1$–$\boldsymbol{\Phi}_r$, and the mode $\boldsymbol{\Phi}_j$ ($j = 1, \ldots, r$) represents the temperature distribution over the grid points G_1–G_m at a specific frequency f_j.

C. Stage-3: ITF Prediction

Normally, only a few modes dominate the ITF dynamic system among the modes $\boldsymbol{\Phi}_1$–$\boldsymbol{\Phi}_r$. To improve computational efficiency, the dominant dynamic modes among $\boldsymbol{\Phi}_1$–$\boldsymbol{\Phi}_r$ are selected to build reduced-order model for ITF prediction. This selection is based on mode energy, which represents the contribution of mode $\boldsymbol{\Phi}_j$ to the ITF dynamic system. Fig. 8 shows the selection of dominant modes among $\boldsymbol{\Phi}_1$–$\boldsymbol{\Phi}_r$ and the ITF prediction by dominant modes, which includes the following Steps 1–3.

Step1: The energy $E_j$of mode $\boldsymbol{\Phi}_j$ can be calculated by the following [25]:

$$E_j = ||\boldsymbol{\Phi}_j||_F^2 \tag{21}$$

where $\|\cdot\|_F$ is the Frobenius paradigm. Based on (12) and (21), Fig. 9 shows the spectrum of modes $\boldsymbol{\Phi}_1$–$\boldsymbol{\Phi}_r$, taking the power loss in (4) with $P_{\mathrm{peak}} = 200\,\mathrm{W}$ and $f_{\mathrm{p}} = 50\,\mathrm{Hz}$ as an example. It can be seen that the 0 Hz mode and 50 Hz mode dominate the ITF dynamic system, and their energies are hundreds of times that of other modes. Here, the 0 Hz mode represents the stabilized

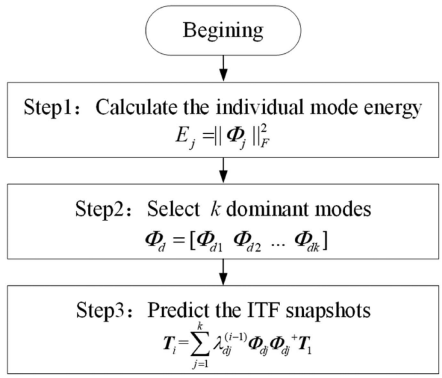

Fig. 8. Dominant modes selection and the ITF prediction.

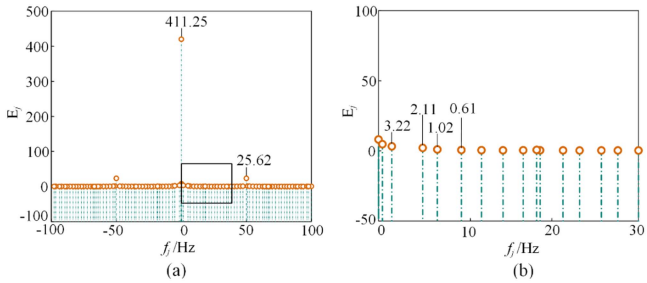

Fig. 9. (a) E_j corresponds to various f_j. (b) Zoom in the black box area.

mode of the ITF and the 50 Hz mode represents the periodic oscillation mode of the ITF.

Step 2: The modes $\boldsymbol{\Phi}_1$, $\boldsymbol{\Phi}_2$, ... $\boldsymbol{\Phi}_r$ are sorted by E_j, and the top k ($1 \le k \le r$) order of modes $\boldsymbol{\Phi}_{d1}$, $\boldsymbol{\Phi}_{d2}$, … $\boldsymbol{\Phi}_{dk}$ are selected as dominant modes to build reduced-order model as follows:

$$\boldsymbol{\Phi}_d = [\boldsymbol{\Phi}_{d1}\boldsymbol{\Phi}_{d2}\ldots\boldsymbol{\Phi}_{dk}]. \tag{22}$$

The ratio ∂, which is the sum of the top k order of dominant modes' energies to the sum of all r order of modes' energies, can be expressed as follows:

$$\partial = \frac{\sum_{j=1}^{k} E_{dj}}{\sum_{j=1}^{r} E_j}, (1 \le k \le r) \tag{23}$$

with

$$E_{dj} = ||\boldsymbol{\Phi}_{dj}||_F^2. \tag{24}$$

From (23), it can be observed that the larger k is, the larger ∂ is.

Step 3: The k order of dominant modes $\boldsymbol{\Phi}_{d1}$–$\boldsymbol{\Phi}_{dk}$ store the main evolution information of ITF, which can be used to predict the evolution trend of ITF beyond the sampling range S_t. Based on (10), (11) and dominate modes $\boldsymbol{\Phi}_{d1}$–$\boldsymbol{\Phi}_{dk}$, $\boldsymbol{T}_{i+1}$ can be obtained from $\boldsymbol{T}_i$, as shown in Fig. 10, and the prediction snapshot at the ith (n+2≤i≤m) instant can be obtained by recursion. Thus, the ith ITF prediction snapshot can be calculated as follows:

$$\boldsymbol{T}_i = \sum_{j=1}^{k} \lambda_{dj}^{(i-1)} \boldsymbol{\Phi}_{dj}\boldsymbol{\Phi}_{dj}{}^{+}\boldsymbol{T}_1, (n+2 \le i \le m). \tag{25}$$

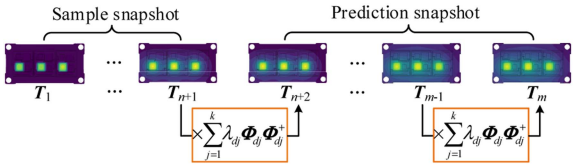

Fig. 10. ITF prediction principle.

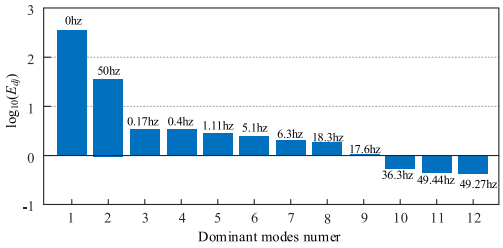

Fig. 11. Logarithm of energy for the first 12 orders of dominant modes.

IV. Discussion of the Proposed Method

The accuracy and computational efficiency of the proposed DMD based RTFP method are discussed in this section. The proposed method is compared with the FEM simulation. The simulation step is set as 0.001 s. The equivalent power loss in (4) with $P_{\text{peak}} = 200$ W and $f_{\text{p}} = 50$ Hz is applied to the FEM simulation. The heat transfer coefficient is used to represent the cooling condition. The relative root mean square error (RRMSE) is used to evaluate the error between the FEM simulation and the proposed method, which is calculated as follows:

$$\text{RRMSE} = \sqrt{\frac{\| \boldsymbol{T}_{\text{FEM}} - \boldsymbol{T}_{\text{DMD}} \|_2^2}{\| \boldsymbol{T}_{\text{FEM}} \|_2^2}} \tag{26}$$

where $\boldsymbol{T}_{\text{DMD}}$ is the ITF snapshot obtained from the proposed method, $\boldsymbol{T}_{\text{FEM}}$ is the ITF snapshot obtained from FEM simulation. $\|\cdot\|$ is the 2-Norm of the matrix. The smaller the RRMSE, the higher the prediction accuracy of the proposed method, and vice versa.

A. *Selection of* Δt *and* S_{t}

According to the sampling theorem [26], the smaller the sampling interval Δt, the larger the sampling range S_t, the more modes information can be captured, but it also increases the computational burden and the time required. According to study [27], in the ITF modeling, due to the slow process of thermal diffusion, the temperature changes in the low-frequency range often contain most of the temperature evolution information, and the accuracy of temperature prediction mainly depends on the low-frequency modes. Fig. 11 shows the logarithm of energy for the first 12 orders of dominant modes. It can be seen that the dominant modes are concentrated between 0 and 50 Hz (power loss frequency). Hence, to ensure that most of the dominant modes are captured, the sampling frequency needs to be more than twice the power loss frequency. Thus, Δt should satisfy that it is half of $1/f_{\text{p}}$ and an integer multiple of the simulation step length.

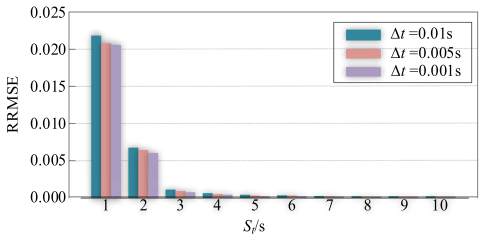

Fig. 12. RRMSE for all prediction snapshots at different S_t and Δt.

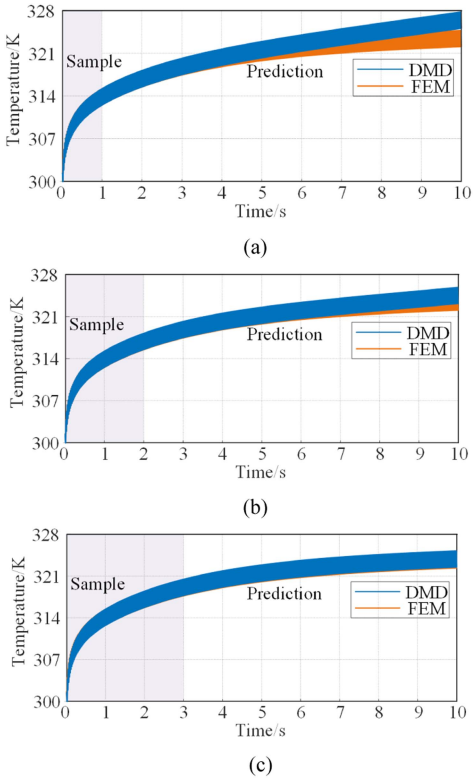

Fig. 13. Comparison of temperatures. (a) $S_t = 1$ s. (b) $S_t = 2$ s. (c) $S_t = 3$ s.

Fig. 12 shows the RRMSE for all prediction snapshots obtained at different S_t and Δt. Obviously, along with the increase of S_t and the decrease of the Δt, RRMSE would be decreased. As S_t increases, RRMSE decreases exponentially for a constant Δt. Conversely, as Δt decreases, the decrease in RRMSE is insignificant for a constant S_t. Thus, S_t has a larger effect on prediction accuracy than Δt. To reduce the computational burden, Δt should be as large as possible without destroying the prediction accuracy. Hence, it is suggested that Δt be set to half of $1/f_{\text{p}}$ (in this case, $\Delta t = 0.01$ s).

To reduce the time for obtaining sample snapshots, S_t should be as small as possible without destroying the prediction accuracy. Fig. 13 shows the temperature data at the center of the chip Q5 (in Fig. 4), which are obtained from the FEM simulation and the proposed method with $S_t = 1, 2, 3$ s. The predicted temperature of the proposed method gradually deviates from the FEM simulation temperature when $S_t = 1$ s and $S_t = 2$ s. The predicted temperature of the proposed method is very close

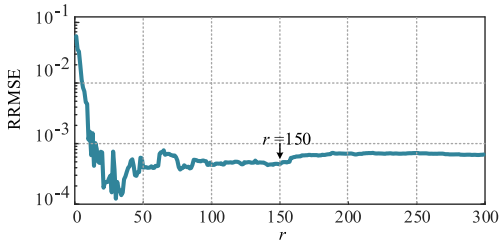

Fig. 14. RRMSE for all prediction snapshots at different values of r.

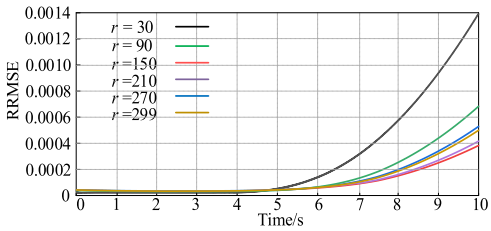

Fig. 15. RRMSE for each prediction snapshot at different values of r.

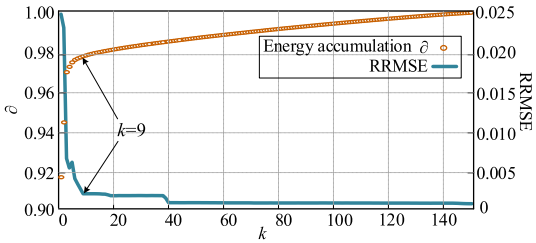

Fig. 16. RRMSE for all prediction snapshots at different values of k.

to the FEM simulation temperature when $S_t = 3$ s. Hence, S_t is recommended to be 3/10 of the prediction range.

B. Selection of r

The truncated SVD for TDM $\boldsymbol{T}_\alpha$ retains r ($1 \le r \le n$) singular values. Too small the value of r will lead to the loss of important spatio-temporal information, while too large the value of r will amplify the influence of noise [25]. Fig. 14 shows the RRMSE for all prediction snapshots at different values of r with $S_t = 3$ s, $\Delta t = 0.01$ s, $n = 299$. It can be seen that the RRMSE remains stable and low when $r \ge 150$. Fig. 15 shows the RRMSE for each prediction snapshot at different values of r. The increasing trend of RRMSE for $r = 30$ and $r = 299$ is steeper than that for $r = 150$. Hence, it is suggested to truncate 50% of the singular values (in this case, $r = 150$).

C. Selection of k

The ITF prediction is based on the k ($1 \le k \le r$) number of dominant modes. Based on (23), the larger the ratio of k/r, the larger energy accumulation ∂, which represents that the modes energy accumulation ∂ increases as the number k of dominant modes selected increases. Fig. 16 shows RRMSE and energy accumulation ∂ at different values of k with $S_t = 3$ s, $\Delta t = 0.01$ s, $r = 150$. It can be seen that as k increases, ∂ gradually approaches 1, and at the same time, RRMSE decreases and tends to stabilize. Hence, ∂ can be used to select the value of k. When ∂ exceeds a threshold value of 0.98, the corresponding value of k can be used in the method to obtain satisfactory prediction results. Hence, to ensure prediction accuracy, k can be selected as 9 for this case.

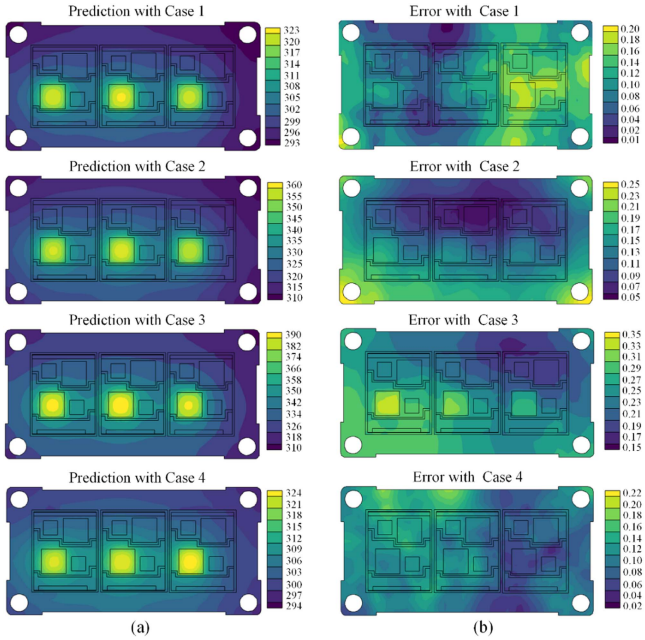

Fig. 17. (a) ITF prediction cloud image at $t = 10$ s. (b) Error cloud image.

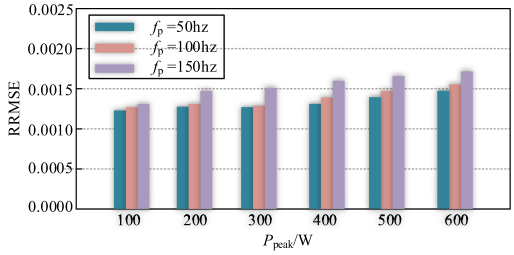

Fig. 18. RRMSE for test cases with different f_p and P_{peak}.

D. Effectiveness Under Different Power Losses

To verify the effectiveness of the proposed method under different equivalent power losses, several typical f_p and P_{peak} are used as test cases. Fig. 17(a) shows the ITF prediction cloud image at $t = 10$ s for four cases: Case 1: $P_{peak} = 200$ W, $f_p = 50$ Hz; Case 2: $P_{peak} = 400$ W, $f_p = 50$ Hz; Case 3: $P_{peak} = 600$ W, $f_p = 50$ Hz; Case 4: $P_{peak} = 200$ W, $f_p = 100$ Hz. Fig. 17(b) shows the corresponding error cloud image with FEM simulation in these four cases. The maximum temperature error is less than 0.5 K, and the errors are relatively uniformly distributed in space. The error results demonstrate that the proposed method can accurately predict the entire ITF.

Fig. 18 shows the RRMSE for different test cases. It can be seen that the prediction accuracy decreases with an increase in f_p or P_{peak}, but the overall error range remains relatively small.

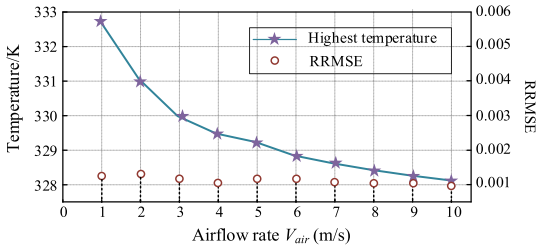

Fig. 19. Highest temperature and RRMSE of ITF under different airflow rates.

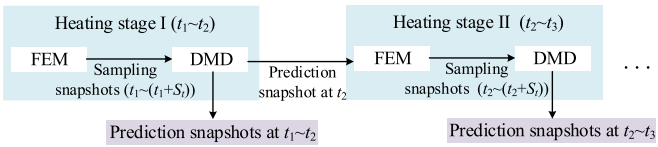

Fig. 20. Process of the proposed method to predict different heating stages within a time series.

E. Effectiveness Under Different Cooling Conditions

To verify the effectiveness of the proposed method under different cooling conditions, ITF predictions are tested under different airflow rates V_{air}. Fig. 19 shows the highest temperature of the ITF at different V_{air}. It can be seen that the highest temperature decreases quickly with the increase of V_{air} between 1 and 5 m/s. However, when the V_{air} is between 6 and 10 m/s, the highest temperature decreases slowly with increasing V_{air}. This may be due to the heat transfer rate approaching saturation at high V_{air}, indicating that the cooling system is approaching the limit of its ability to dissipate heat. Consequently, further increases in wind speed result in only limited temperature reduction. Fig. 19 shows that the RRMSE remains consistently low at different V_{air}. This indicates that the prediction accuracy of the proposed method is not affected by the cooling conditions. In conclusion, the proposed method can be used for ITF prediction under different cooling conditions, providing an excellent tool for designing low-cost and reliable cooling systems for IGBT modules.

F. Effectiveness Under Multiple Heating Stages Within a Time Series

As the heating conditions change, the proposed method can quickly obtain the prediction snapshots for these conditions through corresponding sample snapshots. Fig. 20 shows the process of the proposed method to predict multiple heating stages within a time series (t_1–t_n). In heating stage I (at t_1–t_2), FEM is used to obtain a small number of sample snapshots at (t_1–(t_1+S_t)). Based on these sample snapshots, the proposed method can quickly obtain prediction snapshots for heating stage I. In heating stage II (at t_2–t_3), the prediction snapshot at t_2 obtained by the proposed method is imported into the FEM simulation, and the sample snapshots at (t_2–(t_2+S_t)) for Heating Stage II are obtained by FEM. Then, the proposed method is used to obtain prediction snapshots for heating stage II. As a result, the prediction snapshots for each heating stage can be obtained by the proposed method.

TABLE II
CASE WITH THREE HEATING STAGES

Heating stage	Power loss	RRMSE
I	P_{peak}=100W, f_{p}=50Hz	0.00125
II	P_{peak}=200W, f_{p}=50Hz	0.00121
III	P_{peak}=400W, f_{p}=50Hz	0.00132

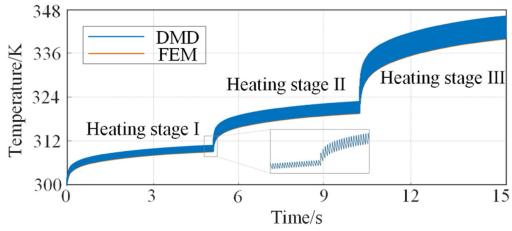

Fig. 21. Prediction results of the three heating stages within a time series.

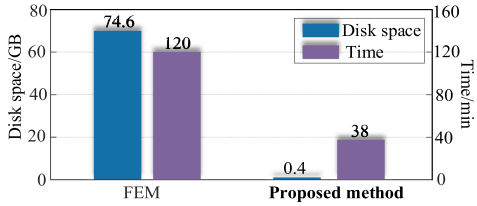

Fig. 22. Comparison of methods.

To verify the proposed method under multiple heating stages within a time series, the case with three heating stages shown in Table II was used for testing. Fig. 21 shows the prediction results of the three heating stages within a time series, and it can be seen that the results of the proposed method are very close to those of the FEM. The RRMSE in Table II indicates that the proposed method works well for multiple heating stages within a time series.

G. Performance Evaluation of the Proposed Method

Fig. 22 shows the results of calculation time comparison between the proposed method and the FEM simulation. To obtain the ITF prediction snapshots for 10 s, the FEM simulation requires 120 min. However, the proposed method only takes 38 min, including the time to obtain sampling snapshot. This effectively reduces the calculation time by 68% and improves the computational efficiency, while maintaining an acceptable error margin, as shown in Section IV-D and IV-E. Fig. 22 shows the results of data storage space comparison between the proposed method and FEM simulation. The FEM requires 10 000 files to be saved for 10-s ITF snapshot, occupying 74.6 GB of disk space. In contrast, the proposed method only requires 9 files to be saved for the dominant modes, occupying 0.4 GB of disk space, thus significantly reducing the disk space occupation by 99% .

H. Comparison With Exiting Methods

Table III compares existing methods with the proposed method. The mathematical methods [28], [29], [30] accelerate FEM computation by reducing the system's degrees of freedom, projecting high-dimensional finite element models onto

TABLE III
COMPARISON WITH EXISTING TEMPERATURE PREDICTION METHODS

Method	Temperature field	Modeling complexity	Accuracy
Mathematical method [28]-[30]	Yes	Complex	High
Deep learning method [31]-[34]	Yes	Complex	Medium
Thermal network model [10]-[14]	No	Complex	Medium
Frequency domain model [35]	No	Medium	Medium
AI-assisted thermal model [36]	No	Medium	Low
Proposed method	Yes	Easy	High

low-dimensional subspaces. Classical projection techniques, such as the proper orthogonal decomposition (POD) method [28], Krylov subspace methods [29], and the Galerkin projection method [30], are widely employed in constructing these models. However, they require computing all mesh point parameters (e.g., thermal capacitance matrix, thermal stiffness matrix), resulting in substantial computational load during modeling. Additionally, these methods demand a deep understanding of high-order control equations. Estimating IGBT temperature fields involving forced air or water cooling necessitates dealing with complex fluid-structure coupling control equations, which presents significant challenges. The deep learning methods [31], [32], [33], [34] mainly construct reduced-order models through data-driven approaches, avoiding the strong reliance on control equations inherent in mathematical methods. Techniques like long short-term memory networks [31], artificial neural networks [32], deep neural networks [33], and Bayesian estimation [34] have been used in combination with the POD method to create noninvasive reduced-order models. However, these methods require large amounts of sample data to ensure prediction accuracy and involve significant training time. The thermal network model in [10], [11], [12], [13], [14], [35], and [36] can only obtain temperatures at measurement points, but the proposed method can obtain the entire ITF. In terms of modeling complexity, the thermal parameters in [10], [11], [12], [13], and [14] increase exponentially with the model order and the number of chips due to the consideration of thermal coupling effects. The method in [35] converts the thermal model to frequency domain solving, reducing computational burden, but it requires an additional transformation process, making the modeling process more complex. The method in [36] uses artificial intelligence (AI) to construct the thermal model, which makes the modeling process relatively simple, but the effectiveness of the model has not been verified in multichip modules. In terms of accuracy, due to the complex coupling effect, the methods in [10], [11], [12], [13], [14], [35], and [36] cannot achieve the predictive accuracy of FEM, but the proposed method almost reaches the same prediction accuracy as FEM. In conclusion, the advantages of the proposed method are that it can predict the entire ITF, is simple to model, and achieves almost the same accuracy as FEM, but takes much less time, which greatly improves the simulation efficiency.

V. EXPERIMENTAL VERIFICATION

The experimental platform is shown in Fig. 23(a). A basic power cycling test circuit topology for the IGBT was used for

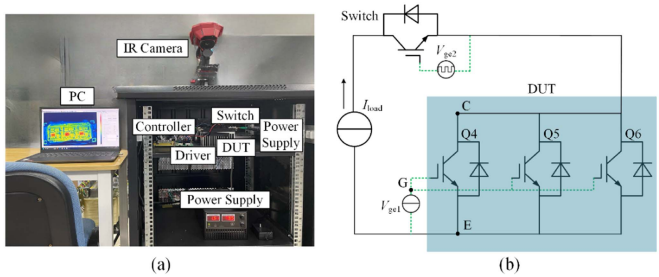

Fig. 23. (a) Experimental setup. (b) Topology of the experimental setup.

TABLE IV
VERIFICATION EXPERIMENT DESCRIPTION

Case	Power loss/w	Frequency/Hz	Duty ratio
I	400	5	0.5
II	200	5	0.5
III	200	0	1
IV	50	0	1

TABLE V
MAXIMUM ERROR FOR FOUR DIFFERENT OPERATION CASES

	Case I	Case II	Case III	Case IV
Maximum error /K	0.5K	0.4K	0.7K	0.5K

the experiment as shown in Fig. 23(b). The device under test (DUT) is an open IGBT module painted black, which is driven to keep it turned on by a constant voltage source. An aluminum heat sink with dimensions of 122 × 62 × 60 mm is installed under the DUT. The surface of the heat sink has dense fins to increase the heat dissipation area, and an axial fan generates a uniform airflow with a velocity of 2 m/s. The power supply outputs a constant current to induce power loss on the DUT. The power loss can be determined by calculating the product of the current and the conduction voltage drop of the DUT.

The amplitude variation of the power loss of the DUT is achieved by changing the output current of the power supply. The frequency variation of the power loss of the DUT is achieved by applying pulsewidth modulation (PWM) signals of different frequencies to the switches. The IR camera was used to record ITF transient processes. Experiments were carried out under four operating cases, including different power losses and PWM signals with different frequencies and duty ratios, as shown in Table IV.

Fig. 24 compares ITF cloud images obtained from the experiments and the proposed method, respectively, where the four cases in Table IV are considered. It can be seen that the ITF cloud images obtained by the proposed method are very close to the experiments. In all four cases, the temperature at the center of chip Q5 is higher than that at the centers of Q4 and Q6, which is mainly due to the thermal coupling effect between the chips [31]. In all four cases, the temperature at the center of Q6 is higher than that at the center of Q4, which may be due to uneven heat dissipation caused by the lack of thermal grease between the heat sink and the IGBT module.

Table V shows the maximum absolute errors between the experiments and the proposed method. The maximum error

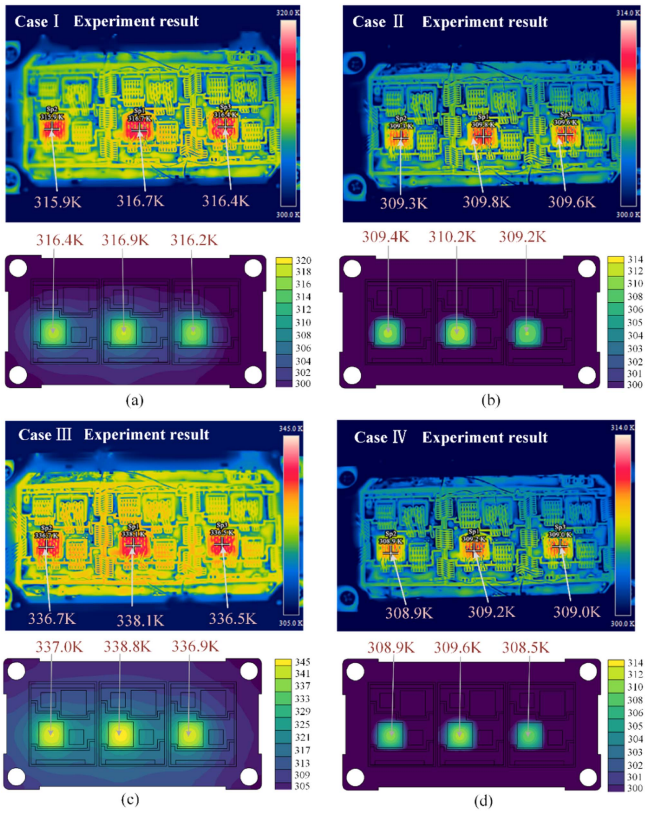

Fig. 24. Comparison results. (a) Case I. (b) Case II. (c) Case III. (d) Case IV.

under the four operation cases is 0.5 K, 0.4 K, 0.7 K, and 0.5 K, respectively. The error may be attributed to the natural convective heat transfer from the surface of the open IGBT module exposed to the air in the experiment. In conclusion, the experimental results are very close to the predicted results.

VI. Conclusion

This article proposes a DMD based RTFP method for IGBT modules. The proposed method requires only a small number of sample snapshots to capture the dynamic modes of the ITF and selects a small number of dominant modes to build a reduced-order model to predict the ITF. The following conclusions are obtained by analyzing the prediction results.

1) To obtain longer and more accurate ITF prediction snapshots, we suggest increasing the sampling range and decreasing the sampling interval, and increasing the sampling range is more effective.
2) To achieve a lower error level, we suggest using a 50% SVD truncation level and modes with energy accumulation exceeding 98% to establish a reduced-order model.
3) The proposed method can reduce the FEM simulation time by 68% and reduces the disk space by 99% .

It is worth mentioning that the proposed method applies not only to the ITF prediction but also to the temperature field prediction of other power electronic devices. The verification results are shown in the Appendix.

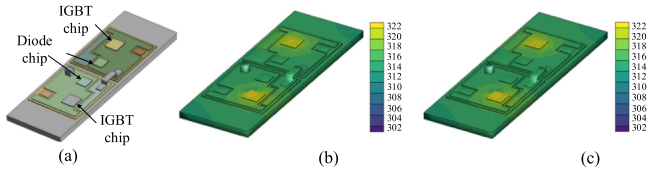

Fig. 25. (a) Finite element model of IGBT module FF50R12RT4. (b) Cloud images from FEM. (c) Cloud images from the proposed method.

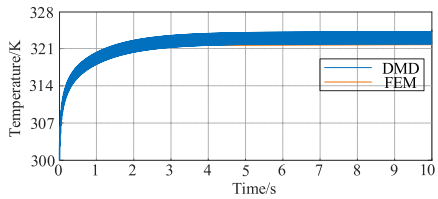

Fig. 26. Transient response curve from FEM and the proposed method.

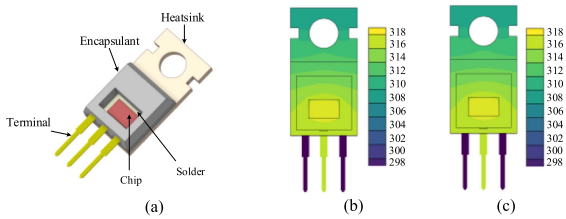

Fig. 27. (a) Finite element model of MOSFET IRF9640N. (b) Cloud image from FEM. (c) Cloud image from the proposed method.

Appendix

A. Verification Case With Other IGBT Module

To validate the effectiveness of the proposed method for different IGBT module structures, another model of IGBT module FF50R12RT4, as shown in Fig. 25(a), was tested. This model includes upper and lower bridge arms, each containing an IGBT chip and a diode chip. The power loss tested was a sinusoidal half wave with $P_{\text{peak}} = 100$ W, $f_{\text{p}} = 50$ Hz. Fig. 25(b) and (c) show the temperature field cloud images calculated using the FEM and the proposed method, respectively. It can be seen that the temperature distributions obtained by both methods are highly consistent. Furthermore, Fig. 26 shows the transient response curve of the highest temperature point, comparing the prediction results of the FEM and the proposed method in the time series. The results show that the temperature predictions of the proposed method almost coincide with those of the FEM, with a maximum temperature difference of less than 0.2 K and a relative error of less than 0.06% . In summary, the proposed method is also effective in ITF prediction with other IGBT modules.

B. Verification Case With Single Tube Power Device

To validate the effectiveness of the proposed method for single tube power devices, a power MOSFET IRF9640N, as shown in Fig. 27(a), was tested. The power MOSFET packaging includes a MOSFET chip mounted on a heatsink through solder. The device is connected to the external circuit through three terminals, and its

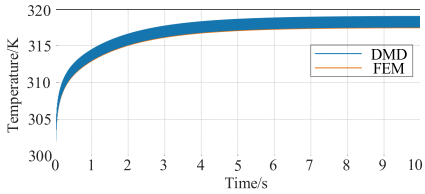

Fig. 28. Transient response curve from FEM and the proposed method.

chip is protected by an encapsulant. The power loss tested was a sinusoidal half wave with $P_{\text{peak}} = 20$ W, $f_{\text{p}} = 50$ Hz. Fig. 27(b) and (c) show the temperature field cloud image distributions obtained using the FEM and the proposed method, respectively. Fig. 28 shows the transient results of the highest temperature point obtained by the FEM and the proposed method. It can be seen that the results of the proposed method are very close to those of the FEM, indicating that the proposed method is also effective for single tube power devices.

REFERENCES

[1] Q. Yu, F. Deng, Y. Tang, X. Cai, Z. Chen, and F. Blaabjerg, "Review of health monitoring techniques for capacitors in modular multilevel converters," *IEEE Trans. Power Electron.*, to be published, doi: 10.1109/TPEL.2025.3571897.

[2] H. Yi, F. Deng, Y. Zhang, B. Li, and Q. Zou, "Bipolar modular AC–AC converter for low-frequency transmission," *IEEE Trans. Power Electron.*, vol. 39, no. 12, pp. 16256–16267, Dec. 2024.

[3] D. Lin, F. Deng, W. Hua, M. Cheng, Z. Chen, and Z. Wang, "High-performance photon-driven PMDC motor system," *Nature Commun.*, vol. 15, no. 1, pp. 1–15, 2024.

[4] J. Wang et al., "A transient 3-D thermal modeling method for IGBT modules considering uneven power losses and cooling conditions," *IEEE J. Emerg. Sel. Topics Power Electron.*, vol. 9, no. 4, pp. 3959–3970, Aug. 2021.

[5] J. Wang et al., "A novel approach to model and analyze uneven temperature distribution among multichip high-power modules and corresponding method to respecify device SOA," *IEEE Trans. Power Electron.*, vol. 37, no. 4, pp. 4626–4640, Apr. 2022.

[6] Y. Duan, F. Xiao, Y. Luo, and F. Iannuzzo, "A lumped-charge approach based physical SPICE-model for high power soft-punch through IGBT," *IEEE J. Emerg. Sel. Topics Power Electron.*, vol. 7, no. 1, pp. 62–70, Mar. 2019.

[7] N. Baker, L. Dupont, S. Munk-Nielsen, F. Iannuzzo, and M. Liserre, "IR camera validation of IGBT junction temperature measurement via peak gate current," *IEEE Trans. Power Electron.*, vol. 32, no. 4, pp. 3099–3111, Apr. 2017.

[8] Y. Guo, H. Yu, Y. Gong, and F. Qin, "Thermal analysis of IGBT by isogeometric boundary element method," in *Proc. 21st Int. Conf. Electron. Packag. Technol.*, 2020, pp. 1–5.

[9] Y. Zhao, E. Deng, M. Pan, Y. Zhang, and Y. Huang, "Influence of thermal coupling on lifetime under power cycling test," *IEEE Trans. Power Electron.*, vol. 37, no. 11, pp. 13641–13651, Nov. 2022.

[10] M. Xu, K. Ma, X. Cai, G. Cao, and Y. Zhang, "Lumped thermal coupling model of multichip power module enabling case temperature as reference node," *IEEE Trans. Power Electron.*, vol. 37, no. 10, pp. 11502–11506, Oct. 2022.

[11] X. Yang, K. Heng, X. Dai, X. Wu, and G. Liu, "A temperature dependent cauer model simulation of IGBT module with analytical thermal impedance characterization," *IEEE J. Emerg. Sel. Topics Power Electron.*, vol. 10, no. 3, pp. 3055–3065, Jun. 2022.

[12] H. Wang et al., "A thermal network model for multichip power modules enabling to characterize the thermal coupling effects," *IEEE Trans. Power Electron.*, vol. 39, no. 5, pp. 6225–6245, May 2024.

[13] W. Guo et al., "Decoupling compact thermal model in multi-chip IGBT modules: A methodology based on concepts of positive and negative mutual thermal coupling," *IEEE J. Emerg. Sel. Topics Power Electron.*, vol. 12, no. 6, pp. 5476–5492, Dec. 2024.

[14] Y. Lu et al., "A 3-D temperature-dependent thermal model of IGBT modules for electric vehicle application considering various boundary conditions," *IEEE J. Emerg. Sel. Topics Power Electron.*, vol. 12, no. 6, pp. 5463–5475, Dec. 2024.

[15] Y. Jia, F. Xiao, Y. Duan, Y. Luo, B. Liu, and Y. Huang, "PSpice-COMSOL-based 3-D electrothermal–mechanical modeling of IGBT power module," *IEEE J. Emerg. Sel. Topics Power Electron.*, vol. 8, no. 4, pp. 4173–4185, Dec. 2020.

[16] Y. Shi, J. Liu, Y. Ai, S. Chen, and Y. Bai, "Dynamic IGBT three-dimensional thermal network model considering base solder degradation and thermal coupling between IGBT chips," *IEEE Trans. Transp. Electrific.*, vol. 9, no. 2, pp. 2994–3011, Jun. 2023.

[17] N. Dornic et al., "Stress-based model for lifetime estimation of bond wire contacts using power cycling tests and finite-element modeling," *IEEE J. Emerg. Sel. Topics Power Electron.*, vol. 7, no. 3, pp. 1659–1667, Sep. 2019.

[18] B. Wang et al., "Air-cooling system optimization for IGBT modules in MMC using embedded O-shaped heat pipes," *IEEE J. Emerg. Sel. Topics Power Electron.*, vol. 9, no. 4, pp. 3992–4003, Aug. 2021.

[19] T. Wu, Z. Wang, B. Ozpineci, M. Chinthavali, and S. Campbell, "Automated heatsink optimization for air-cooled power semiconductor modules," *IEEE Trans. Power Electron.*, vol. 34, no. 6, pp. 5027–5031, Jun. 2019.

[20] R. D. Rodriguez-Soto, E. Barocio, F. Gonzalez-Longatt, F. R. Segundo Sevilla, and P. Korba, "Robust three-stage dynamic mode decomposition for analysis of power system oscillations," *IEEE Trans. Power Syst.*, vol. 39, no. 2, pp. 4000–4009, Mar. 2024.

[21] J. Wang, W. Chen, Y. Wu, J. Zhang, L. Wang, and J. Liu, "Chip-level electrothermal stress calculation method of high-power IGBT modules in system-level simulation," *IEEE Trans. Power Electron.*, vol. 37, no. 9, pp. 10546–10561, Sep. 2022.

[22] C. Entzminger, W. Qiao, L. Qu, and J. L. Hudgins, "Automated extraction of low-order thermal model with controllable error bounds for SiC MOSFET power modules," *IEEE Trans. Power Electron.*, vol. 39, no. 1, pp. 538–551, Jan. 2024.

[23] Z. Khatir, R. Lallemand, A. Ibrahim, and D. Ingrosso, "Thermal stress analysis comparison in IGBT power modules between DC and switching power cycling," *IEEE Trans. Power Electron.*, vol. 38, no. 9, pp. 11500–11506, Sep. 2023.

[24] Y. Zhang, H. Wang, Z. Wang, Y. Yang, and F. Blaabjerg, "Simplified thermal modeling for IGBT modules with periodic power loss profiles in modular multilevel converters," *IEEE Trans. Ind. Electron.*, vol. 66, no. 3, pp. 2323–2332, Mar. 2019.

[25] Y. Xu et al., "A data-driven koopman approach for power system nonlinear dynamic observability analysis," *IEEE Trans. Power Syst.*, vol. 39, no. 2, pp. 4090–4104, Mar. 2024.

[26] M. Xu, K. Ma, B. Liu, and X. Cai, "Modeling and correlation of two thermal paths in frequency-domain thermal impedance model of power module," *IEEE J. Emerg. Sel. Topics Power Electron.*, vol. 9, no. 4, pp. 3971–3981, Aug. 2021.

[27] M. Xu, K. Ma, Q. Zhong, and M. Liserre, "Frequency-domain thermal modeling of power modules based on heat flow spectrum analysis," *IEEE Trans. Power Electron.*, vol. 38, no. 2, pp. 2446–2455, Feb. 2023.

[28] Y. Zhao, Z. Wang, D. Luo, C. Chen, B. Ji, and G. Li, "Multitimescale thermal network model of power devices based on POD algorithm," *IEEE Trans. Power Electron.*, vol. 39, no. 4, pp. 3906–3924, Apr. 2024.

[29] X. Dong, A. Griffo, and J. Wang, "Multiparameter model order reduction for thermal modeling of power electronics," *IEEE Trans. Power Electron.*, vol. 35, no. 8, pp. 8550–8558, Aug. 2020.

[30] G. Fan, X. Li, and M. Canova, "A reduced-order electrochemical model of Li-Ion batteries for control and estimation applications," *IEEE Trans. Veh. Technol.*, vol. 67, no. 1, pp. 76–91, Jan. 2018.

[31] L. Zhou et al., "High-fidelity wind turbine wake velocity prediction by surrogate model based on d-POD and LSTM," *Energy*, vol. 275, no. 15, 2023, Art. no. 127525.

[32] M. Allabou, R. Bouclier, P. Garambois, and J. Monnier, "Reduction of the shallow water system by an error aware POD-neural network method: Application to floodplain dynamics," *Comput. Methods Appl. Mechan. Eng.*, vol. 428, no. 1, 2024, Art. no. 117094.

[33] X. Zhao et al., "A hybrid method based on proper orthogonal decomposition and deep neural networks for flow and heat field reconstruction," *Expert Syst. Appl.*, vol. 247, no. 1, 2024, Art. no. 123137.

[34] M. Guo, S. McQuarrie, and K. Willcox, "Bayesian operator inference for data-driven reduced-order modeling," *Comput. Methods Appl. Mechan. Eng.*, vol. 402, no. 1, 2022, Art. no. 115336.

[35] M. Xu et al., "Frequency-domain thermal coupling model of multi-chip power module," *IEEE Trans. Power Electron.*, vol. 38, no. 5, pp. 6522–6532, May 2023.
[36] Y. Zhang, Z. Wang, H. Wang, and F. Blaabjerg, "Artificial intelligence-aided thermal model considering cross-coupling effects," *IEEE Trans. Power Electron.*, vol. 35, no. 10, pp. 9998–10002, Oct. 2020.
[37] A. Wintrich, N. Ulrich, T. Werner, and T. Reimann, *Application Manual Power Semiconductors*. Nuremberg, Germany: Semikron, 2015.

Jiahao Geng received the M.S. degree in electrical engineering from Henan Polytechnic University, Jiaozuo, China, in 2021. He is currently working toward the Ph.D. degree in electrical engineering in the School of Electrical Engineering, Southeast University, Nanjing, China.

His research interests include thermal modeling and reliability analysis of power devices, and multilevel converter control in renewable energy systems.

Fujin Deng (Senior Member, IEEE) received the B.Eng. degree in electrical engineering from the China University of Mining and Technology, Jiangsu, China, in 2005, the M.Sc. degree in electrical engineering from Shanghai Jiao Tong University, Shanghai, China, in 2008, and the Ph.D. degree in energy technology from the Department of Energy Technology, Aalborg University, Aalborg, Denmark, in 2012.

From 2013 to 2015, he was a Postdoctoral Researcher and from 2015 to 2017, he was an Assistant Professor, with the Department of Energy Technology, Aalborg University. He joined the Southeast University in 2017 as a Professor with the School of Electrical Engineering, Southeast University, Nanjing, China. His main research interests include wind power generation, multilevel converters, high-voltage direct-current technology, dc grid, and offshore wind farm-power systems dynamics.

Kai Hou was born in 1981, Jiangsu, China. He received the Ph.D. degree in physical electronics from Southeast University, Nanjing, China, in 2010.

He is currently a Senior Engineer and Graduate Student tutor in NARI group corporation, SGCC. He was an Academic Visitor of Department of Engineering, University of Cambridge, during 2008–2009. He is currently the General Manager of Nanjing NARI New Energy Technology Company, Ltd.

Qiang Yu received the B.Eng. degree in electrical engineering from Jilin University, Changchun, China, in 2017, and the Ph.D. degree in electrical engineering from Southeast University, Nanjing, China, in 2023.

From 2022 to 2023, he was a visiting Ph.D. student in the School of Electrical and Electronic Engineering, Nanyang Technological University, Singapore. He is currently working with Southeast University as a Postdoctoral Researcher. His research interests include modular multilevel converters and their applications.

Yaqian Zhang (Member, IEEE) received the B.S. degree from the University of Electronic Science and Technology of China, Chengdu, China, in 2016, and the Ph.D. degree from Southeast University, Nanjing, China, in 2023, both in electrical engineering.

During 2021–2022, she was a visiting Ph.D. student in the Department of Energy Technology, Aalborg University, Aalborg, Denmark. She is currently a Lecturer with Southeast University. Her research interests include medium- and high-voltage power electronic converters including modular multilevel converter and the solid-state transformer.

Yeyuan Xie was born in April 1978. He received the B.S. degree in power systems and automation and the M.S. degree in power electronics and power transmission from Zhejiang University, Hangzhou, China, in 1998 and 2006, respectively.

He is a professor-level Senior Engineer, works with NR Electric Company Ltd., Nanjing, China, and has been engaged in flexible dc/ac transmission technology for a long time.

Mr. Xie has been a member of CIGRE DC Transmission China region and is a member of the expert group in the field of electric equipment of the National Industrial Foundation Expert Committee since 2020.

Jun Mei (Member, IEEE) was born in Jinan, Shandong, China, in 1997. He received the B.S. degree in electrical engineering and automation engineering from the Shandong University of Aeronautics, Binzhou, China, in 2019, and the M.S. degree in power system and automation from the Hunan University of Technology, Zhuzhou, China, in 2022. He is currently working toward the Ph.D. degree in electrical engineering in Southeast University, Nanjing, China.

His research interests include renewable energy power conversion and grid connection technology, ac/dc microgrid control technology, and HVDC.

Guangtai Zhang was born in 1979 in Shandong, China. He received the M.S. degree in mechanical design and theory from Southeast University, Nanjing, China, in 2005.

He is currently the Deputy General Manager of Changzhou Borui Power Automation Equipment Company Ltd., Changzhou, China, specializing in the engineering application of intelligent power equipment technologies.